using the BOLPs-RGp. The position and intensity of activity were measured during the 200 s immediately after proton irradiation using the trigger signal of the beam-off time. The measurement was performed using the shortest possible distance between the two opposing detector heads of the BOLPs-RGp for each patient. The average distance of the detector heads was 40 cm for the head and neck and the brain, 70 cm for the liver and the lungs, and 50 cm for the prostate. The time of 200 s after proton beam irradiation was chosen according to the intensity of activity estimated from the results of other studies (10, 13). The activity data obtained during proton irradiation were not used for PET imaging. Various types of background radiation (X-rays, gamma rays, and neutrons) occur during proton beam irradiation, and the quality of the activity image becomes markedly worse in their presence (2, 10, 15, 16). Furthermore, high radiation decreases the accuracy of the detector.

Verification of activity measurement was performed in 18, 4, 15, 10, and 1 cases involving tumors of the head and neck, the liver, the lungs, the prostate, and the brain, respectively. The typical fractional dose is 2.5 Gy equivalents (GyE = Gy × the relative biologic effectiveness: [= 1.1 = constant]) for the head and neck, 3.8 GyE for the liver, 4.0 GyE for the lungs, 2.0 GyE for the prostate, and 2.5 GyE for the brain in our facility. The irradiated field is typically planned with three fields in the head and neck and two fields in other sites. Furthermore, the typical number of irradiated field per fractional dose is one in the head and neck, liver, and prostate, and two in the lungs. The fractional dose was delivered over an irradiation time of 10–300 s. The proton beam irradiation was synchronized with the organ motion caused by respiration in the liver and the lungs.

Procedure for clinical use of activity image

A flow chart of procedure for clinical use of the BOLPs-RGp is shown in Fig. 2. In the clinical use, the main operation is to take an activity image every day and compare the activity image of the first day of treatment with each activity image during the comparatively long period of the treatment. If the difference of both the images is confirmed by reducing of the tumor size and changing of the body shape, then the new dose distribution is obtained from redose calculation of the plan on a new CT image acquisition, and the first proton treatment plan is immediately corrected to the new plan. As a result, proton treatments of high accuracy can be offered to the patient by keeping of the planned dose delivery.

RESULTS

Estimation of the measurement time for PET imaging

An estimation of an appropriate measurement time for PET imaging was performed using the measured activity data from tumors of the head and neck. The proton beam conditions were as follows: an energy of 120 MeV, a spread out of Bragg peak (SOBP) of 80-mm width, a gantry angle of 340°, a fractional dose of 2.5 GyE, and an irradiation time of 24 s. The distance between the detector heads was 70 cm, and the detection rate of the activity was 1.5 kcps. The left panel of Fig. 3 shows the number of detection events per volume during the detection period after proton beam irradiation. The statistical error (= standard deviation/mean value) decreased as the detection time increased. The error was 2.8% for a 200-s detection time, 3.0% for 150 s, 3.4% for 100 s, and 4.4% for 50 s. The right panel of Fig. 3 shows
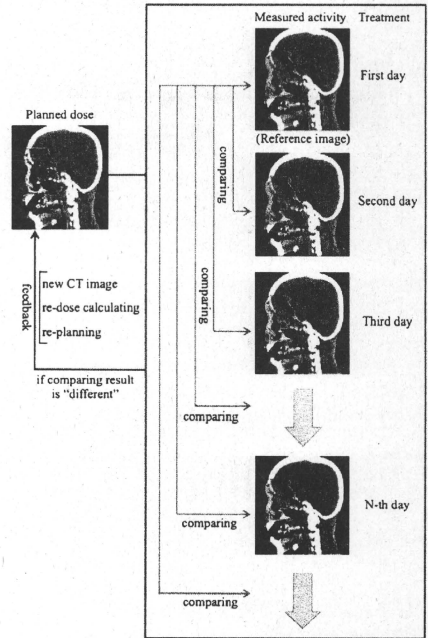

Fig. 2. Flow diagram of the procedure for the clinical use of the BOLPs-RGp.

PET images taken using detection times of (a) 0, (b) 50, (c) 100, and (d) 200 s.

PET images of each treatment site

Typical PET images obtained by the BOLPs-RGp are shown for each case involving tumors of the head and neck, the liver, the lungs, the prostate, and the brain. Figure 4 shows the calculated dose distribution and the measured activity distribution on the first treatment day. The beam irradiation parameters were shown in Table 1. The PET images were obtained during the 200 s after proton beam irradiation. The mean detection rates of the activity generated in the proton beam irradiated volume were 1.58, 1.39, 0.53, 1.08, and 1.85 kcps, respectively. The color line and wash normalized to the iso-center show the dose distribution and activity distribution, respectively. By comparing and verifying between the calculated dose distribution and the measured activity distribution, it can be confirmed visually and roughly that the proton beam has irradiated the tumor. In cases of the liver and the lungs, the length of beam irradiation time is adjusted according to the stability of respiration on the treatment day and the patient. By the effect of organ motion, the number of
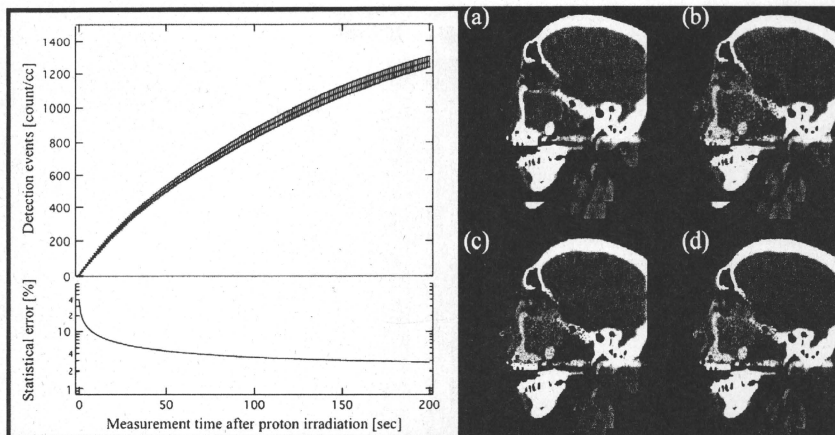
Fig. 3. The number of detection events per volume and PET images obtained during the detection period after proton beam irradiation. The PET images for detection period of (a) 0, (b) 50, (c) 100, and (d) 200 s are shown.

the detection event of the activity measured in the gating window will became about one third of the total detection events, and the statistical error will increase. Therefore, the measurement was performed with no synchronization with organ motion by respiration.

Changes in the activity distribution during the treatment period

In each treatment site, the activity distribution changed probably by reduction of the tumor size and changing of the body shape was conspicuously observed in some cases of the head and neck.

The verification was performed for a case involving tumors of the head and neck. Proton beam irradiation was performed in three fields of view: Port 1: 123 MeV, 90-mm SOBP, 350° gantry angle, 0° bed angle; Port 2: 121 MeV, 90-mm SOBP, 10° gantry angle, 20° bed angle; and Port 3: 117 MeV, 80-mm SOBP, 340° gantry angle, 350° bed angle. The irradiation dose was 2.5 GyE. Figure 5 shows a calculated proton dose distribution, an activity distribution, and a depth profile of a 2.5-GyE dose irradiation after a delivery dose of 2.5 (reference image), 10.0, 17.5, or 32.5 GyE from Port 1, a delivery dose of 5.0 (reference image), 12.5, 20.0, or 35.0 GyE, from Port 2, and a delivery dose of 7.5 (reference image), 15.0, 22.5, or 30.0 GyE from Port 3. Changes of the activity distribution were observed according to changes of the proton beam range and the dose delivered by previous irradiations resulted in a reduction of the tumor (see the arrow and the area surrounded by the dotted line in Fig. 5). The changing values of the activity range for each irradiation field (Port 1, Port 2, and Port 3) are shown in upper left of Fig. 6.

The activity range was defined by the depth point of 50% distal falloff in the activity distribution normalized at the iso-center. The changing value of the activity range fully exceeded a 10-mm length. Moreover, to observe the changes in the activity distribution in the depth direction in a similar manner, the ratio of the integration of the detected numbers between 20 mm and 70 mm from the iso-center was expressed as follows:

$$R(D) = \frac{\int_{20}^{70} \left(dA(D)/dZ \right) dz}{\int_{20}^{70} \left(dA(0)/dZ \right) dz}. \quad (1)$$

Here, z is the depth, D is the delivery dose, A(D) is the depth activity distribution, and A(0) is the reference depth activity distribution. The ratio of the delivery dose is shown in the middle left of Fig. 6. The bottom left of Fig. 6 is the proton beam irradiation time per fraction dose at each irradiation. The average of the irradiation time was 30 s, and the difference of the irradiation time at random was within 3 s.

In this case, a new CT image was scanned and a retreatment planning was produced after the delivery of 35 GyE of the prescribed dose of 65 GyE. The volume of the tumor was decreased from 184 mL to 125 mL (the arrow in right of Fig. 6 shows the visible tumor reduction), and the maximum beam range was shortened by 20-mm water equivalent length. In the other 2 cases of 18 clinical cases of the head and neck, the changing activity range of more than 10 mm was observed. Similarly, the new CT image acquisition and the retreatment planning were immediately performed after the observation of the changing activity range. The reduction
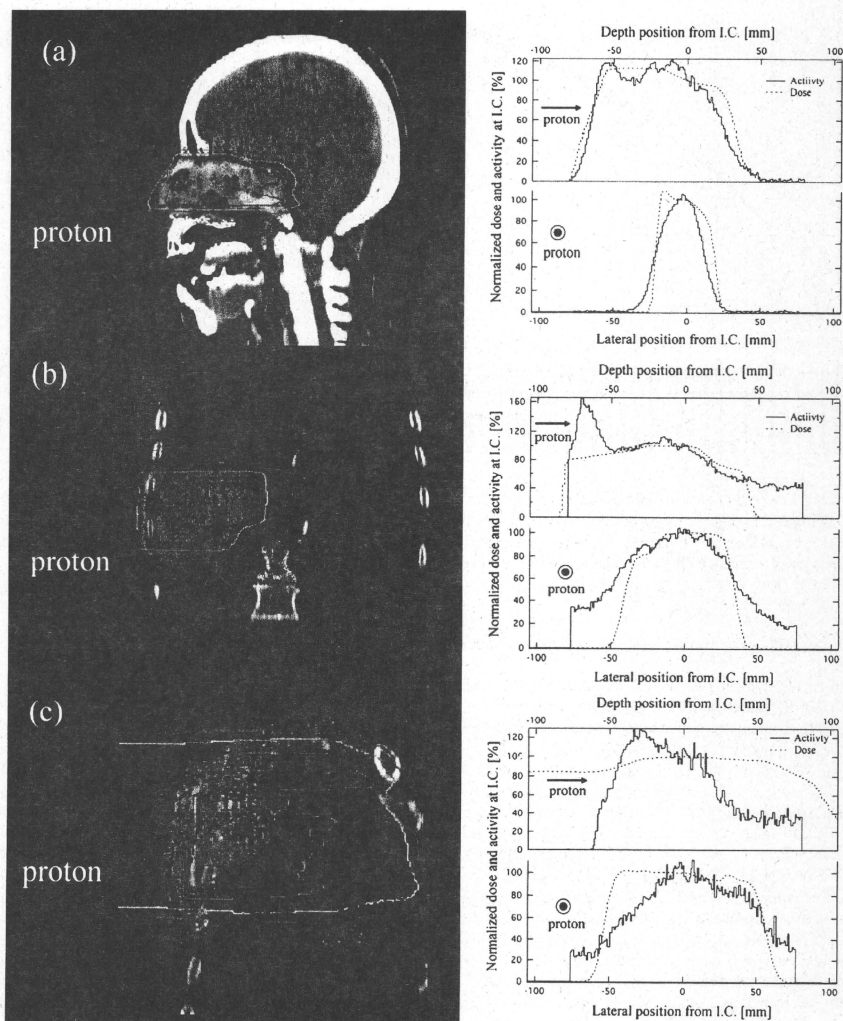
Fig. 4. The calculated dose distribution and the measured activity distribution (left figure), and corresponding lateral and depth profiles (right figure) of the irradiation fields (see Table 1) in each case involving tumors of the head and neck (a), the liver (b), the lungs (c), the prostate (d), and the brain (e), respectively. The iso-dose line of 100% is red, 80% yellowish green, 50% light blue, and 20% purple. The iso-activity wash between 30% and 100% changed from light blue to red.
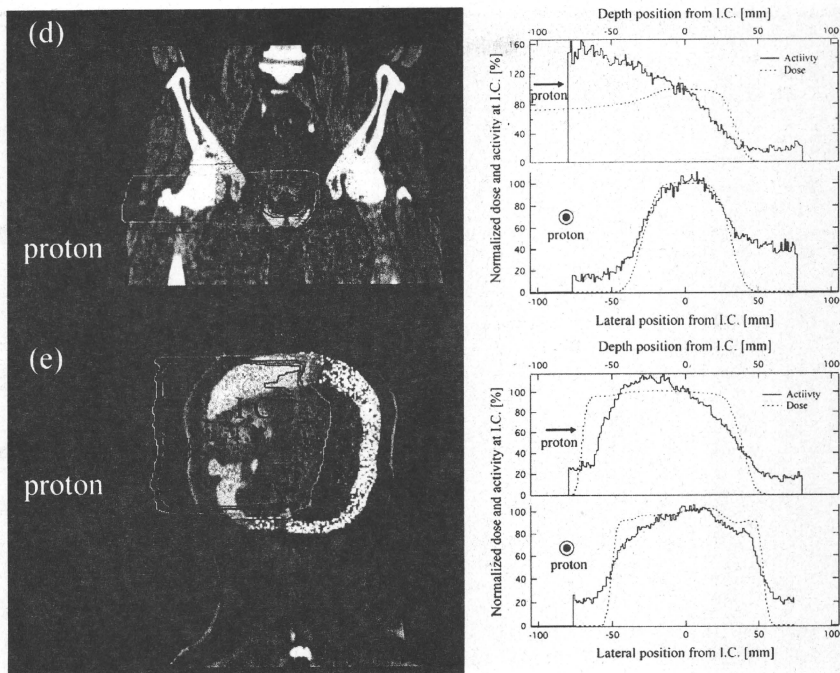
Fig. 4. (*continued*).

of the tumor's volume was more than 100 mL. Also, in carbon therapy, similar observation of the tumor shrinkage has been reported in (7). The BOLPs-RGp indicated that the proton irradiation dose was delivered to the brain stem of organs at risk.

Washout effect of the activity in the treatment period

A histopathologic examination demonstrated that higher activity was observed in regions containing necrotic liver cells than in any other region. The upper panel of Fig. 7 shows the calculated dose distribution and the measured activity distribution on a CT image taken at the first treatment of a 3.8 GyE delivery dose. The bottom left panel of Fig. 7

shows the number of detection counts per 20 s of activity in the regions of interest of areas A and B in the liver. Hence, the region of interest of area A is the necrotic region of the tumor, and area B is the normal tumor region. Therefore, area B-A is equivalent to the area of the tumor minus the necrotic region. The observed decay curves in the region of interest of area A and B-A were fitted well enough using a double exponential equation. The two half-lives of the double exponential fitting were 31 ± 8 s and 146 ± 20 s in the area A, and 21 ± 4 s and 164 ± 11 s in the area B-A, respectively. The half-life was longest in the necrotic region of the tumor. The activity images for the 200 s measurement by the BOLPs-RGp are shown in the left of Fig. 8. The high activity

Table 1. Summary of proton beam irradiation parameters

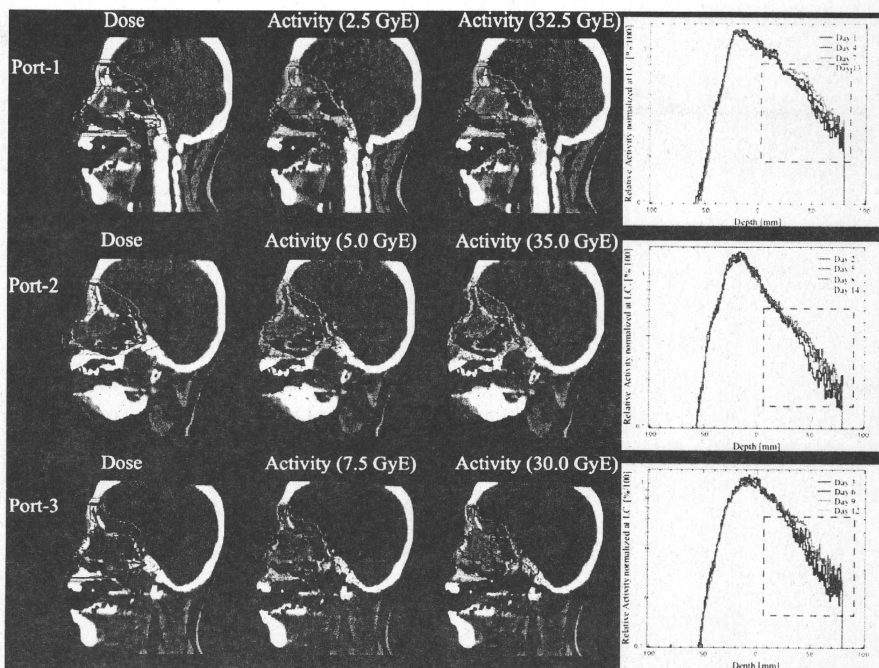|	Treatment site	Proton energy [MeV]	SOBP [mm]	Gantry angle [deg.]	Bed angle [deg.]	Fractional dose [GyE]	Irradiation time [sec.]
(a)	Head and Neck	123	90	0	0	2.5	39
(b)	Liver	137	70	270	0	3.8	229
(c)	Lungs	145	70	160	0	2.0	38
(d)	Prostate	187	50	270	0	2.0	15
(e)	Brain	122	90	330	90	2.5	40

Fig. 5. The calculated proton dose distribution, measured activity distribution of a 2.5-GyE dose irradiation, and the depth profile of the measured activity normalized to the iso-center (0-mm depth) of the reference activity after a delivery dose of 2.5–35.0 GyE.

of the necrotic region decreased to same level as the normal parts of the liver in the last treatment. The ratio F of the detection activity normalized to the activity data from the first treatment for the delivery doses in the area A and the area B-A is expressed as follows:

$$F(D) = \frac{\int_0^{S_A} \left(d\mathrm{N(D)}/dS \right) dS / \int_0^{S_A} dS}{\int_{S_A}^{S_B} \left(d\mathrm{N(D)}/dS \right) dS / \int_{S_A}^{S_B} dS}. \quad (2)$$

Here, N is the detection number, S_A is the square of area A, and S_B is the square of area B. Ratio of the F values normalized at the value in first treatment calculated by using Eq. 2 and proton beam irradiation time per fraction dose are shown in the right of Fig. 8. The average of the irradiation time at random was 159 ± 77 s. There was no correction in the irradiation time and the decrease of the activity shown in Fig. 8. A decrease in the activity of the necrotic region was observed after the delivery dose was increased without depending on the beam irradiation time per fraction dose.

DISCUSSION

This study focused on the development of the BOLPs-RGp and its clinical use against tumors of the head and neck, lungs, prostate, and brain in the proton therapy. Quick measurement of the activity generated in a patient's body after proton irradiation is feasible by using the BOLPs-RGp. The elements tracked by the activity imaging are ^{11}C (20.39 min), ^{10}C (19.26 s), ^{13}N (9.965 min), ^{15}O (122.2 s), ^{14}O (70.61 s), ^{30}P (2.498 min), and ^{38}K (7.636 min), and according to the results of a simulation by Parodi *et al.*, the "key" positron emitter nuclei are ^{11}C and ^{15}O (14). The measurement of this activity must be immediately performed after proton irradiation as the half-life of ^{15}O is about 2 min. As a result, the information for activity imaging is obtained in a short period. On the other hand, in the case of a beam OFF-LINE PET system used with a commercial based PET or PET/CT apparatus, it is very difficult to measure the activity of ^{15}O for several minutes even at the start of the activity measurement after proton irradiation. The main elements used for activity imaging are ^{15}O for measurements with
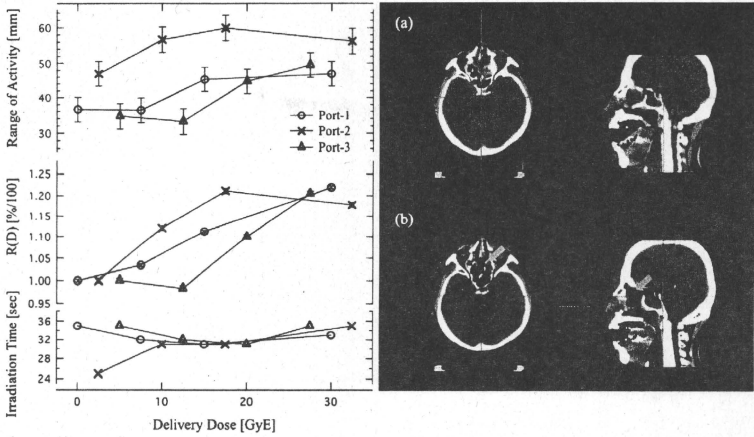
Fig. 6. Changes in the values of the activity range and proton beam irradiation time per fraction dose at each irradiation field of Port-1, Port-2, and Port-3. Axial and sagittal CT images of the head and neck before treatment (a) and after delivery doses of 35 GyE (b).
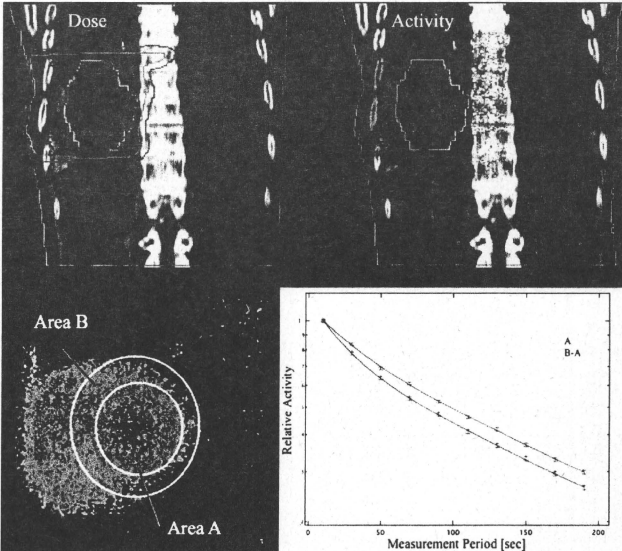

Fig. 7. The calculated dose distribution and the measured activity distribution on a CT image after the first treatment with a 3.8-GyE delivery dose, and the number of detection counts per 20 seconds of the activity in the region of interest (ROI) of areas A and B in the liver.
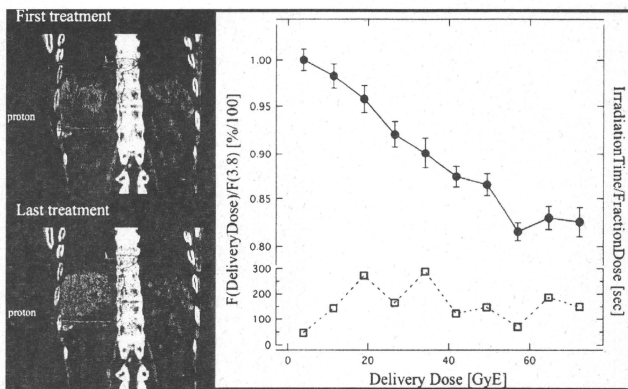
Fig. 8. The activity image and the ratio of the detection number to the measured activity calculated according to Equation (2) in the necrotic region of the liver tumor, and proton beam irradiation time per fractional dose.

the BOLPs-RGp and ^{11}C for measurements with the beam OFF-LINE PET system. As a tumor is equivalent to soft tissue, the measurement of the many [15]O nuclei generated in a tumor by proton irradiation is very important for the observation and evaluation of the changing form and the delivery dose response of the tumor. [12]C is present and ^{11}C is generated in the adipose tissue. Therefore, high activity is indicated in the region under the skin when using the beam OFF-LINE PET system. Furthermore, the BOLPs-RGp has the advantage of taking measurements with the patient in same position during proton irradiation. However, the CT image for the patient positioning can not be acquired at the same time as the activity measurement when using the BOLPs-RGp. This problem can be solved by the technological introduction of a CBCT.

At present, the length of activity measurement with the BOLPs-RGp after proton beam irradiation is 200 s; but, it may be possible that the measurement time can be shortened to less than 200 s as a result of this research. However, the measurement time must be determined with consideration to the detection efficiency by the delivery dose of each treatment site, the distance between the detector heads, and the activity measurement synchronized with the organ motion caused by respiration in the case of the liver and lungs.

The BOLPs-RGp has been used in the daily proton treatment of 48 patients. The monitoring of the accuracy of the proton beam irradiation was performed by comparing and verifying the daily activity images with reference activity images obtained at the start of the proton treatment. Specially, optimized proton treatment was performed by quickly replanning treatment in three clinical cases involving head-and-neck tumors, because different activity distribution were observed in the two images during the treatment period. The decrease of the activity in the region of necrotic cells in the liver tumor found during the histopathological examina-

tion was linked to an increase in the delivery dose. It is suggested that the increase in the washout effect in the necrotic region is caused by a decrease in the number of necrotic cells in the liver because of increased blood flow caused by the higher proton delivery dose. This effect may indicate a need to adapt the treatment to the dose response of the tumors in individual patients as well as the observation of the functional metabolism of organs.

The quality of the activity image is reduced by the large organ motion of the liver and the lungs. In cases of the prostate, the verification of changes in the activity distribution against the condition of the bladder and the position of the head of the femur will be reported in future. Moreover, a study concerning the experimental determination of cross sections of the target nuclear fragment reaction has been completed, and a simulation system that includes our cross-section data for calculating activity distribution in a patient's body with a high accuracy has been constructed using a cluster computer system. Many results of the research of the simulation have been already reported by the study group of Parodi *et al.* (12, 14). Finally, the ideal DGPT will be achieved through these developments and the research.

CONCLUSIONS

A BOLPs-RGp was constructed in our proton treatment room. The BOLPs-RGp has been used in many clinical cases. Report of the clinical use with beam ON-LINE PET or in-beam PET in the proton therapy has been never done before. The daily activity images obtained indicated the proton irradiation volume of the treatment administered to patients. Information about the positron-emitting nuclei provided by the BOLPs-RGp will be important for improving proton treatment accuracy in the future. DGPT (10) will thereby be achieved via daily proton treatment using the BOLPs-RGp.

REFERENCES

1. Oelfke U, Lam G, Atkins M. Proton dose monitoring with PET: Quantitative studies in Lucite. *Phys Med Biol* 1996;41:177–196.
2. Litzenberg DW, Roberts DA, Lee MY, *et al*. On-line monitoring of radiotherapy beams: Experimental results with proton beams. *Med Phys* 1999;26:992–1006.
3. Parodi K, Enghardt W. Potential application of PET in quality assurance of proton therapy. *Phys Med Biol* 2000;45:N151–N156.
4. Nishio T, Ogino T, Shimbo M, *et al*. Distributions of b⁺ decayed nucleus produced from the target fragment reaction in $(CH_2)n$ and patient liver targets by using a proton beam for therapy. *Abstr XXXIV PTCOG Mtg Boston* 2001;15–16.
5. Parodi K, Enghardt W, Haberer T. In-beam PET measurements of β^+ radioactivity induced by proton beams. *Phys Med Biol* 2002;47:21–36.
6. Hishikawa Y, Kagawa K, Murakami M, *et al*. Usefulness of positron-emission tomographic images after proton therapy. *Int J Radiat Oncol Biol Phys* 2002;53:1388–1391.
7. Enghardt W, Parodi K, Crespo P, *et al*. Dose quantification from in-beam positron emission tomography. *Radiother Oncol Suppl 2* 2004;73:S96–S98.
8. Nishio T, Sato T, Kitamura H, *et al*. Distributions of β^+ decayed nuclei generated in the CH_2 and H_2O targets by the target nuclear fragment reaction using therapeutic MONO and SOBP proton beam. *Med Phys* 2005;32:1070–1082.
9. Parodi K, Ponisch F, Enghardt W. Experimental study on the feasibility of in-beam PET for accurate monitoring of proton therapy. *IEEE Trans Nucl Sci* 2005;52:778–786.
10. Nishio T, Ogino T, Nomura K, *et al*. Dose-volume delivery guided proton therapy using beam ON-LINE PET system. *Med Phys* 2006;33:4190–4197.
11. Parodi K, Paganetti H, Cascio E, *et al*. PET/CT imaging for treatment verification after proton therapy: A study with plastic phantoms and metallic implants. *Med Phys* 2007;34:419–435.
12. Parodi K, Paganetti H, Shih HA, *et al*. Patient study of in vivo verification of beam delivery and range, using positron emission tomography and computed tomography imaging after proton therapy. *Int J Radiat Oncol Biol Phys* 2007;68:920–934.
13. Nishio T, Miyatake A, Inoue K, *et al*. Experimental verification of proton beam monitoring in a human body by use of activity image of positron-emitting nuclei generated by nuclear fragmentation reaction. *Radiol Phys Technol* 2008;1:44–54.
14. Parodi K, Ferrari A, Sommerer F, *et al*. Clinical CT-based calculations of dose and positron emitter distributions in proton therapy using the FLUKA Monte Carlo code. *Phys Med Biol* 2007;52:3369–3387.
15. Pawelke J, Enghardt W, Haberer T, *et al*. In-beam PET imaging for the control of heavy-ion tumour therapy. *IEEE Trans Nucl Sci* 1997;44:1492–1498.
16. Parodi K, Ponisch F, Eickhoff H, *et al*. Random coincidences during in-beam PET measurements at microbunched therapeutic ion beams. *Nucl Instrum Meth A* 2005;545:446–458.
17. Uchida H, Okamoto T, Ohmura T, *et al*. A compact planar positron imaging system. *Nucl Instr Meth* 2004;A516:564–574.

Improved dose-calculation accuracy in proton treatment planning using a simplified Monte Carlo method verified with three-dimensional measurements in an anthropomorphic phantom

Kenji Hotta[1], Ryosuke Kohno[2], Yoshihisa Takada[1], Yousuke Hara[1], Ryohei Tansho[1], Takeshi Himukai[3], Satoru Kameoka[2], Taeko Matsuura[2], Teiji Nishio[2] and Takashi Ogino[2]

[1] Institute of Applied Physics, University of Tsukuba, 1-1-1 Tennoudai, Tsukuba, Ibaraki 305-8573, Japan
[2] National Cancer Center Hospital East, 6-5-1, Kashiwanoha, Kashiwa, Chiba 277-8577, Japan
[3] National Institute of Radiological Sciences, 4-9-1, Anagawa, Inage, Chiba, 263-8555, Japan

E-mail: y-takada@bk.tsukuba.ac.jp

Abstract

Treatment planning for proton tumor therapy requires a fast and accurate dose-calculation method. We have implemented a simplified Monte Carlo (SMC) method in the treatment planning system of the National Cancer Center Hospital East for the double-scattering beam delivery scheme. The SMC method takes into account the scattering effect in materials more accurately than the pencil beam algorithm by tracking individual proton paths. We confirmed that the SMC method reproduced measured dose distributions in a heterogeneous slab phantom better than the pencil beam method. When applied to a complex anthropomorphic phantom, the SMC method reproduced the measured dose distribution well, satisfying an accuracy tolerance of 3 mm and 3% in the gamma index analysis. The SMC method required approximately 30 min to complete the calculation over a target volume of 500 cc, much less than the time required for the full Monte Carlo calculation. The SMC method is a candidate for a practical calculation technique with sufficient accuracy for clinical application.

(Some figures in this article are in colour only in the electronic version)

1. Introduction

In proton tumor therapy, tumor control while sparing adjacent organs requires a good treatment plan to maximize dose delivery to the target volume. The optimum plan is formulated by

evaluating the calculation results for a variety of beam configurations. The dose-calculation method must be fast and accurate.

Many facilities currently use pencil beam algorithms (PBAs) (Petti 1992, Hong 1996, Szymanowski 2001) for treatment planning. The required calculation time is relatively short and the accuracy of these algorithms is reasonable when the tumor is surrounded by structures of intermediate complexity. PBAs express the dose distribution formed by a mono-energetic proton pencil beam as a product of the depth-dose distribution in water obtained from measurements or Monte Carlo calculations and an off-axis radial function defined as a two-dimensional Gaussian function with an rms value determined by scattering in the materials along its central axis. The dose distributions of multiple pencil beams at various incident positions and energies are summed to obtain the dose distribution in the patient. Kohno *et al* developed a Range-Modulated-Pencil-Beam Algorithm (RMPBA) to shorten the calculation time while maintaining accuracy by using a measured depth-dose distribution for the combined beam rather than summing the contribution of protons at each specific energy (Kohno 2001).

Though PBAs perform well for homogeneous targets, the accuracy is decreased in targets with large lateral heterogeneity. Since the PBAs assume that the central axis is a straight line and determine the energy deposit and the lateral spread due to materials along the central axis, they do not include the effects of lateral density heterogeneity on the dose distribution. The PBAs also use a zero-thickness collimator approximation ignoring the edge scattering in the aperture collimator. These limitations decrease the dose-calculation accuracy of PBAs in heterogeneous media. In order to improve accuracy, Kanematsu *et al* developed a PBA variant that subdivides the pencil beam kernels into sub-pencil beams when it encounters a large heterogeneity (Kanematsu 2009).

The clinical application of full Monte Carlo calculations such as MCNPX (Waters 2002) or Geant4 (Agostinelli 2003) has been investigated (Paganetti 2008). Although they are capable of more accurately computing dose distribution, they require a long calculation time, up to 6 h per patient even using more powerful cluster machine than ours (Paganetti 2008). To reduce the calculation time, fast pseudo-Monte-Carlo algorithms were proposed (Li 2005, Yepes 2009).

Sakae *et al* (2000) developed a simplified Monte Carlo (SMC) method to obtain fast and accurate dose calculation in heterogeneous targets, and the accuracy of the method in simple targets was verified by Kohno *et al* (2002, 2003). Since the SMC method tracks individual particles, it includes lateral density heterogeneity effects on the dose distribution. A second advantage of the SMC method is easy implementation since it can use same input data for PBAs.

We implemented the SMC method in the clinical treatment planning system of the National Cancer Center Hospital East (NCCHE, Japan). We demonstrated the effectiveness of the SMC method by comparing the calculation results with measurement results in a heterogeneous slab phantom, and that in an anthropomorphic phantom simulating the complexity encountered in a clinical situation. The SMC results were also compared to RMPBA calculations. The data were analyzed using a number of methods, including a variant of the γ-index method (Low 1998) with an accuracy tolerance of 3 mm and 3%.

2. Materials and methods

2.1. Calculation model

A right-handed Cartesian system was used for dose-calculation coordinates in which the central beam axis coincided with the z-axis and the gantry rotated about the y-axis. Target data

in the original CT coordinate system were transformed into the dose-calculation coordinate system using the gantry and couch rotation angles.

The SMC method begins tracking individual protons at the entrance to the range compensator (RC). The initial beam parameters were provided by the effective-source model with the model parameters determined by measurements (Hong 1996, Symanovski 2001). The model provides the standard deviation of the initial angular distribution at any point on the entrance plane. The proton fluence distribution was based on the lateral-dose distribution measured without the RC and aperture collimator. In the system arrangement at the NCCHE, the RC is placed upstream of a patient-aperture collimator. For calculation of range loss and scattering of individual protons in material, polyethylene RC and 60 mm thick brass aperture collimator were divided into segments with a thickness of 1 mm along the z-axis. Patient volume was divided into cubic voxels with twice the edge length of the CT pixels. Each particle was characterized in terms of position, the direction expressed by the two projection angles, and the residual range in water. The trajectory of each particle was tracked by assuming multiple Coulomb scattering with scattered projection angles expressed as a normal random number with a standard deviation calculated using the Highland formula (Highland 1975, 1979). The energy loss of a proton in a segment of material was calculated using the water equivalent model (Chen 1979). We assumed that the relative dose deposit in a patient voxel could be obtained from the measured depth-dose distribution in water. One reason for the shorter calculation time of the SMC method compared with full Monte Carlo methods is the simplification in which the dose deposit in materials is calculated using the measured depth-dose distribution for a mono-energetic proton beam in water, and ignoring absorption and lateral scattering due to nuclear reaction. Note that use of the measured depth-dose curve in water implicitly includes some averaged effects from nuclear interactions.

The calculation method was compared to the RMPBA with the measured effective source model.

2.2. Experiment

We verified the calculation accuracy of the SMC method by comparing the calculation results with the measured dose distributions in the heterogeneous phantoms described in sections 2.2.1 and 2.2.2. The proton beam was extracted from the 235 MeV cyclotron at the NCCHE. For some experiments the energy was reduced using the energy-selection-system (ESS), and the beam was transferred to a passive beam spreading system using the double-scattering method (Nishio 1999, Tachikawa 1999).

A PTW 2D Array seven29™ was used for dose detection. This is a two-dimensional detector matrix containing 729 ionization chambers in a 10 mm pitch 27×27 array developed by ®PTW Freiburg GmbH. Spezi reported the successful application of this detector to radiation therapy and verified the performance (Spezi 2005). The sensitive volume of a unit chamber is 5 mm $\times$ 5 mm $\times$ 5 mm. The ionization chambers of the array are open to the air. The offset thickness from the entrance surface to the center of the sensitive volume is 8 mm in WEL.

To compare the calculation results and measurements under the same conditions, we corrected the calculation of depths by the offset thickness when calculating the dose distributions. We also convolved the calculation results with the detector cell size of 5 mm $\times$ 5 mm.

2.2.1. Slab phantom.
The heterogeneous slab phantom depicted in figure 1 was used for evaluation of the SMC method. We investigated lateral density heterogeneity effects on dose
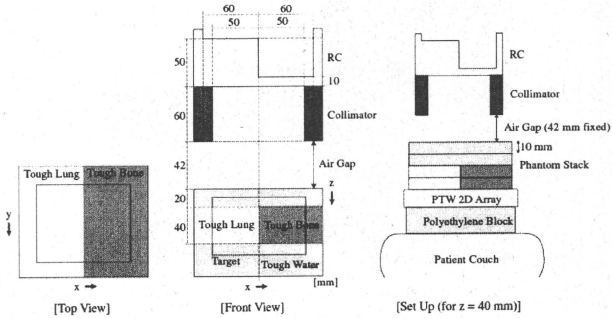
Figure 1. Experimental arrangement of heterogeneous slab phantom, RC and aperture collimator. The red line indicates the target region.

distribution using a 150 MeV proton beam passing through a ridge filter with a spread-out Bragg peak (SOBP) width of 80 mm. The phantom was constructed by combining 10 mm thick component slabs made from Tough Water (TW), Tough Lung (TL), and Tough Bone (TB) (®Kyoto Kagaku Co., Ltd). The water-equivalent–thickness ratios (Takada 2008) of TW, TL and TB are 1.01, 0.34 and 1.40, respectively. We designed the RC and the aperture collimator for the cube-shaped target with a volume of 800 cc (indicated by the red line in figure 1).

Lateral dose distributions were measured at depths of $z = 0$ mm, 20 mm, 40 mm, 60 mm, 80 mm and 90 mm. A stack of the phantom slabs was mounted on the detector to measure the dose distribution in each depth as shown in figure 1. When a different phantom stack was mounted, we fixed the distance between the aperture collimator and the phantom entrance surface by adjusting the vertical position of the patient couch. Since the chamber pitch was 10 mm, we shifted the detector by 5 mm in the x and y directions to obtain measurements with a lateral sampling pitch of 5 mm. Each measurement was repeated three times at each depth and averaged to obtain the lateral-dose distribution.

The simulation required approximately 40 min with a target voxel size of 1 mm per side using 1.14×10^8 generated protons on four cores (two dual-core 2.4 GHz AMD Opteron CPUs, four jobs running in parallel). All the dose data sets were normalized at a point ($x = 30$ mm, $y = 60$ mm) in a flat dose region for comparison of measurements and calculations. The estimated mean statistical error of the calculated dose in the target region was 1% rms, and that of the convolved calculated dose was 0.2% rms. Reduction of the error in the convolved calculated dose came from the larger voxel size.

2.2.2. RANDO phantom. We used the head portion from a RANDO® phantom produced by the Phantom Laboratory® to simulate the complex arrangement of materials experienced in clinical applications. The RANDO phantom mimics the density distribution in the human head using resins with various compositions. Figure 2 contains the median sagittal and median horizontal CT images and the PTV. The phantom is composed of horizontal layers of 25 mm thick. We measured the dose distributions in the layers with the z-index numbered from 1
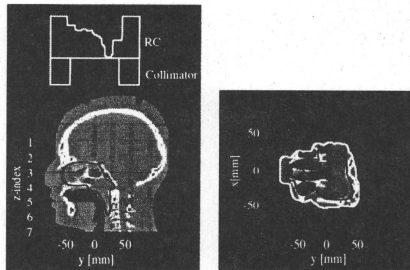
Figure 2. Median sagittal and median horizontal CT images of the head portion from the RANDO phantom. The iso-center (red cross), PTV (red line) and RC and collimator shape (white line) are also depicted.

to 7 as shown in the figure. To simulate clinical situations, we followed the actual patient treatment procedure: obtaining a CT, delineating the PTV, determining the beam direction, manufacturing the corresponding RC and aperture collimator, aligning the reference surface markers on the phantom with laser cross-hairs and irradiating the phantom on the patient couch. We designed a treatment plan assuming a head and neck cancer with a volume of approximately 500 cc. The smearing distance of the RC (Kooy 2008) was taken at 4.5 mm. Since the measurement plane was limited to the horizontal plane due to the layered structure of the phantom, the irradiation direction was also limited to downward from the top of the head. Although the results have no clinical significance due to the unrealistic selection of the irradiation direction, it simulates the dose distribution in the complex heterogeneous region typically found in the head and neck cases.

We used a 235 MeV proton beam with a SOBP width of 80 mm. We mounted a stack of phantom layers on the detector to measure the dose distribution in each measurement plane. The distance between the aperture collimator and the phantom entrance surface was fixed by adjusting the couch height, again. The reported results are the average of three measurements. To estimate the effect of set-up errors on the dose distribution, we repeated the set-up and measurement procedure three times on the $z = 4$ layer where a complicated lateral-dose distribution was expected.

The simulation required approximately 30 min when the target voxel size was 1.17 mm on a side and the number of generated particles was 4.68×10^7 on four cores (two dual-core 2.4 GHz AMD Opteron CPUs, four jobs running in parallel). All the dose data sets were normalized with reference to the dose at the iso-center for comparison. The estimated mean statistical error of the calculated dose in the target region was 1.2% rms, and that of the convolved calculated dose was 0.25% rms.

3. Results

3.1. Slab phantom

Figure 2 compares the iso-dose distributions obtained from (a) measurements, (b) the SMC calculation and (c) the RMPBA calculation. In the figure, we note that the high-dose region
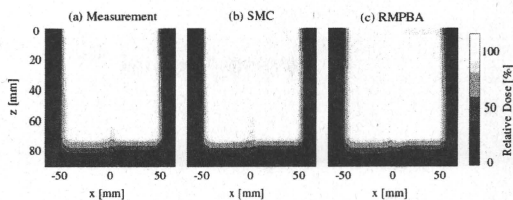
Figure 3. Iso-dose distributions in the heterogeneous slab phantom from (a) measurements, (b) the SMC and (c) the RMPBA. The measurements were obtained at $z = 0$ mm, 20 mm, 40 mm, 60 mm, 80 mm and 90 mm.
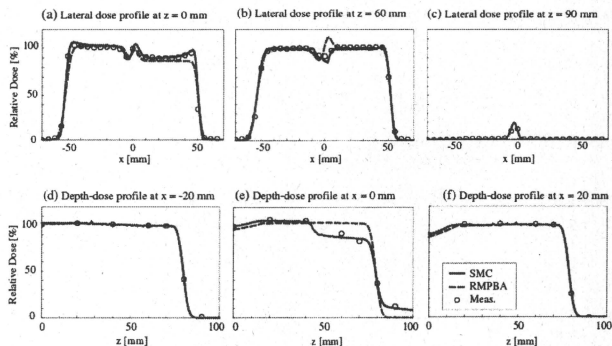

Figure 4. Dose profiles in the heterogeneous slab phantom: solid lines indicate the SMC prediction, dashed lines indicate the RMPBA prediction, and open circles represent measurements. Figures (a)–(c) are lateral-dose profiles at $z = 0$ mm, 60 mm and 90 mm. Figures (d)–(f) are depth-dose profiles at $y = -20$ mm, 0 mm and 20 mm. Since the estimated measurement error from three measurements in each set-up is less than 1.0%p-p of the normalization dose, error bars are not displayed (smaller than circles).

around $x = 0$ mm extends to a region deeper than 50 mm only in the RMPBA. Such differences of dose distribution are shown more clearly in lateral- and depth-dose profiles of figure 4. The SMC method reproduced the measurement results better than the RMPBA in three regions. The first is the peripheral high-dose region around $x = \pm 50$ mm in figure 4(a) that is influenced by the scattered and energy-degraded protons interacting with the edge of the aperture collimator. The SMC method accurately reproduced the measured dose distribution, while the RMPBA does not take into account edge-scattered proton paths and cannot reproduce the dose distribution well in this region. The second region is a dose reduction at depths between $z = 40$ mm and $z = 70$ mm in the vicinity of $x = 0$ mm (figures 4(b) and (e)). This area is influenced by protons passing through both the thicker section of the RC and the
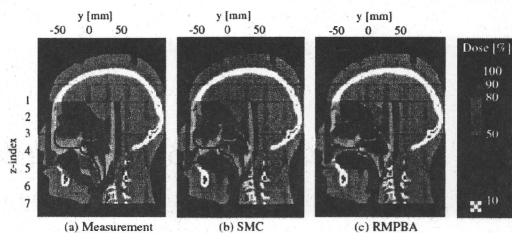
Figure 5. Median sagittal iso-dose distributions in the anthropomorphic phantom from (a) measurements, (b) the SMC and (c) the RMPBA.
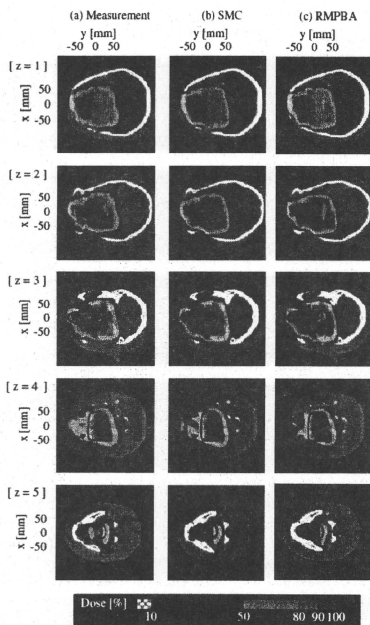

Figure 6. Horizontal iso-dose distributions in the anthropomorphic phantom. The red lines show the target region.
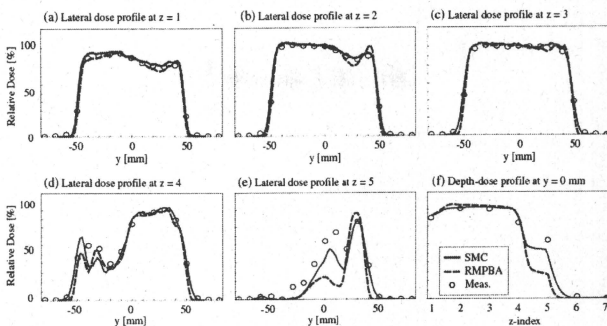
Figure 7. Lateral- and depth-dose profiles in the anthropomorphic phantom. The solid lines depict calculation results using the SMC, the dashed lines depict calculation results from the RMPBA, and the hollow circles represent measurements. Figures (a)–(e) are lateral-dose profiles on the $z = 1$, 2, 3, 4 and 5 levels, and figure (f) is a depth-dose profile at $y = 0$ mm. Since the estimated measurement error from three measurements in each set-up is less than 1.3%p-p of the normalization dose, error bars are not displayed (smaller than circles).

higher-density region in the phantom. The third region is a low-dose region near $x = 0$ mm at a depth of $z = 90$ mm (figures 4(c) and (e)) formed by protons passing through both the thinner section of the RC and the lower-density region in the phantom. Note that this region is located deeper than the target distal boundary. The RMPBA could not reproduce the dose in this region due to the disregard of irregular proton paths mentioned above while the SMC could.

Both the SMC and the RMPBA perfectly reproduced the depth-dose distribution in the region lacking lateral heterogeneity (figures 4(d) and (f)). The difference in calculation accuracy between the SMC and the RMPBA in figure 4(e) was caused by the difference in operation between the two algorithms; the SMC method tracks almost all proton paths while some paths in the RMPBA are missing.

3.2. RANDO phantom

Figures 5 and 6 describe the iso-dose distributions in the median sagittal plane and horizontal planes obtained using (a) measurements, (b) the SMC calculation and (c) the RMPBA calculation. We ignored the $z = 6$ and $z = 7$ planes because almost no protons reached these levels. The number of measurement points irradiated with more than 10% of the normalization dose was 80, 82, 88, 88 and 41 for $z = 1$ through 5. Apparent discrepancy between the target distal boundary and the dose distal boundary can be attributed to difference between the displayed depth and the measured depth by the detector with a cover thickness of 8 mm WEL. Since our interest is focused on difference between measurements and calculations, this is not a major issue here. In the figures, you will note that both the SMC and the RMPBA reproduced the overall measured distribution in some accuracy. Yet there are some local differences shown in dose profiles of figure 7: (a)–(e) are lateral profiles at $z = 1$–5, and (f) is a distal profile at
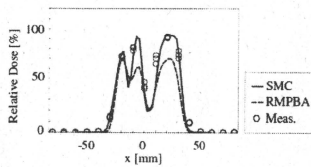
Figure 8. Effect of alignment error on dose distribution in the anthropomorphic phantom along the x-axis at $y = -20$ mm on the $z = 4$ layer. The dose errors caused by set-up misalignment are large at $x = 10$ mm and $x = 30$ mm where the dose gradient is large. Since the estimated measurement error from times measurements in each set-up is less than 0.7%p-p of the normalization dose, error bars are not displayed (smaller than circles).
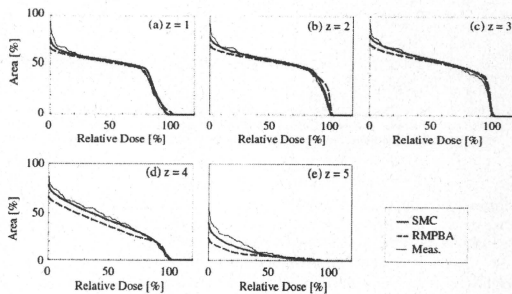

Figure 9. Comparison of dose-surface histograms in each plane from measurements, SMC calculation and PBA calculation. The black solid lines depict the measurement data, the red solid lines depict the SMC results and the blue dashed lines depict the RMPBA results.

$y = 0$ mm. Figures 4(a)–(c) show that both calculations reproduce measurements well with minor local differences. In contrast, we note large discrepancy between measurements and calculations and difference between the SMC and the RMPBA in a part of figures 4(d)–(f). The discrepancy between measurements and calculations is caused by the range uncertainty of the phantom and the large dose gradient in the distal fall-off part of the Bragg curve. The difference between the SMC and the RMPBA notably found in figures 4(e) and (f) is caused by the fact that the RMPBA disregards dose contribution of protons passing through the irregular paths along the phantom and reaching the deep region and underestimates the dose in the deep region.

We also examined the dose error caused by misalignment of the RC, aperture collimator, phantom and detector. Figure 8 depicts three lateral-dose profiles on the $z = 4$ layer of the head phantom following three separate set-up procedures. The figure also contains the SMC and the RMPBA calculation results for the case of no set-up error. The $z = 4$ layer was selected since it includes a region with a large dose gradient in the lateral direction that is
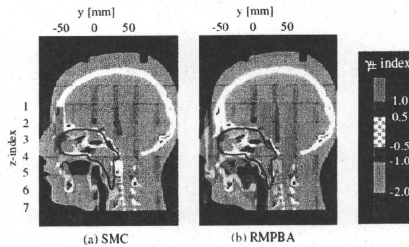
Figure 10. The $\gamma_\pm$-index distributions in the median sagittal plane of the anthropomorphic phantom from (a) the SMC and (b) the RMPBA. The RMPBA exhibits a larger underestimated region than the SMC.

sensitive to set-up error. The measured dose error due to misalignment was a maximum of 9.2%p-p of the normalization dose. Such a large dose error can be attributed to an estimated set-up error of ±0.5 mm and the large dose gradient. The misalignment error is consistent with error of the alignment system using laser cross-hairs.

Figure 8 compares the dose-surface histograms (DSH) obtained from measurements, the SMC calculation and the RMPBA calculation in each measurement plane. The SMC method is superior to the RMPBA, which underestimates the dose in deeper regions. The difference in calculation accuracy between the two algorithms arises from consideration or disregard of irregular proton paths in heterogeneous media. The dose underestimation observed in the $z = 5$ layer even by SMC is caused by uncertainty in the CT-value-to-range conversion and by the large low-density region representing the oral cavity present in this layer. Since most protons in this region have a small residual range, the dose in this region is very sensitive to small uncertainties in the proton range.

4. Discussion

We evaluated the calculation accuracy using the γ-index method (Low 1998). This method simultaneously evaluates the dose difference and the distance to agreement quantitatively. We newly defined a signed-gamma-index ($\gamma_\pm$-index) at each measurement position to differentiate between overestimation and underestimation of the dose:

$$\gamma_\pm(r_m) = \frac{D_c(r_m) - D_m(r_m)}{|D_c(r_m) - D_m(r_m)|} \times \min_{r_c} \left[\sqrt{\frac{(D_c(r_c) - D_m(r_m))^2}{D_{\text{tolerance}}^2} + \frac{(r_c - r_m)^2}{r_{\text{tolerance}}^2}} \right], \quad (1)$$

where D_m and D_c represent the measured and calculated doses, r_c and r_m are the calculated and measured positions, and the parameters $D_{\text{tolerance}}$ and $r_{\text{tolerance}}$ are the tolerance error values of the dose and the distance. The acceptable error in proton therapy dose calculation for heterogeneous targets is not clearly defined at present. We followed the recommendations of Low (1998) for photon therapy, and used 3% for $D_{\text{tolerance}}$ and 3 mm for $r_{\text{tolerance}}$ in this paper. We also defined the pass rate as the fraction of calculation points satisfying the condition of $-1 < \gamma_\pm < 1$.
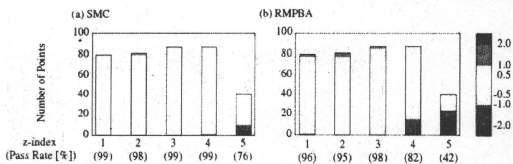
Figure 11. $\gamma_{\pm}$-index histogram for (a) the SMC and (b) the RMPBA. The $\gamma_{\pm}$-index in the stacked bar chart is shown in decreasing order from top to bottom. The number of points contained in a range of signed gamma index is indicated by the height of each bar. The pass rate is printed under the z-index.

Figure 10 illustrates the $\gamma_{\pm}$-index distributions on the median sagittal plane for (a) the SMC and (b) the RMPBA. Figure 5 contains stacked bar charts representing the $\gamma_{\pm}$-index for (a) the SMC and (b) the RMPBA. We expressed the $\gamma_{\pm}$-index scale using various intensities of red to highlight positive regions and blue for negative regions. The color intensity is proportional to the absolute value of the $\gamma_{\pm}$-index. The pass rates in individual horizontal planes are also indicated under the z-index of the measurement planes. While calculation results obtained using the SMC method agreed well with the measurement results for layers $z = 1$–4, the pass rates for the RMPBA method fell below 90% in the $z = 4$ and 5 layers due to underestimation of the dose. Therefore, the SMC method is superior in the calculation accuracy to the RMPBA. Since the SMC method can accurately reproduce the measured dose distribution in complex media within a reasonable calculation time, it is capable of improving the accuracy of dose calculations in clinical situations.

5. Conclusion

We implemented the SMC method in the treatment planning system of the NCCHE in order to improve dose-calculation accuracy in heterogeneous targets. The SMC method is easy to implement because it can use the same input data for PBAs. We verified the effectiveness of the SMC method by comparing the calculation results to the dose distributions measured at different depths in a heterogeneous slab phantom using a two-dimensional detector. We also measured the dose distributions at seven horizontal planes in an anthropomorphic phantom. For both these cases, we found that the SMC method reproduced the measured dose distributions better than the RMPBA. In the slab phantom, we found that the RMPBA overestimated the dose in shallow regions and underestimated the dose in deep regions due to disregard of some proton paths in the heterogeneous region. The same tendency was also found for the RMPBA dose calculations for the anthropomorphic phantom. Since PBAs fundamentally have a risk of disregarding some proton paths, they may underestimate the dose in deep region for the case with large heterogeneity around the target.

We evaluated the treatment plan using the $\gamma_{\pm}$-index analysis and found that the SMC method reproduced the measured dose distributions well within the accuracy tolerance of 3 mm and 3% in almost all regions. In addition, the calculation time required for the SMC method was about 30 min for a typical clinical case (target volume of 500 cc). The SMC method provides the higher calculation accuracy than RMPBA within a reasonable time, even for such a complex case. Since verification of the effectiveness of the SMC method is required

for many clinical cases, we have begun a retrospective comparison between the SMC and PBA methods using previous proton therapy cases.

Acknowledgments

References

Agostinelli S *et al* 2003 GEANT4: a simulation toolkit *Nucl. Instrum. Methods. Phys. Res.* A 506 250–303
Chen G T, Singh R P, Castro J R, Lyman J T and Quivey J M 1979 Treatment planning for heavy ion radiotherapy *Int. J. Radiat. Oncol. Biol. Phys.* 5 1809–19
Highland V L 1975 Some practical remarks on multiple scattering *Nucl. Instrum. Methods* 129 497–9
Highland V L 1979 Some practical remarks on multiple scattering *Nucl. Instrum. Methods* 161 171
Hong L *et al* 1996 A pencil beam algorithm for proton dose calculations *Phys. Med. Biol.* 41 1305–30
Kanematsu N, Komori M, Yonai S and Ishizaki A 2009 Dynamic splitting of Gaussian pencil beams in heterogeneity-correction algorithms for radiotherapy with heavy charged particles *Phys. Med. Biol.* 54 2015–27
Kohno R *et al* 2001 Range-modulated pencil beam algorithm for proton dose calculations *Jpn. J. Appl. Phys.* 40 5187–93
Kohno R *et al* 2002 Simplified Monte Carlo dose calculation for therapeutic proton beams *Jpn. J. Appl. Phys.* 41 L294–7
Kohno R *et al* 2003 Experimental evaluation of validity of simplified Monte Carlo method in proton dose calculations *Phys. Med. Biol.* 48 1277–88
Kooy H M, Trofimov A, Engelsman M and Smith A R 2008 Treatment planning *Proton and Charged Particle Radiotherapy* ed T F Delaney and H M Kooy (Philadelphia, PA: Lippincott Williams & Wilkins) chapter 8, pp 70–107
Li J S, Shahine B, Fourkal E and Ma C M 2005 A particle track-repeating algorithm for proton beam dose calculation *Phys. Med. Biol.* 50 1001–10
Low D A, Harms W B, Mutic S and Purdy J A 1998 A technique for the quantitative evaluation of dose distributions *Med. Phys.* 25 656–61
Nishio T *et al* 2006 Development of a simple control system for uniform proton dose distribution in a dual-ring double scattering method *Phys. Med. Biol.* 51 1249–60
Paganetti H *et al* 2008 Clinical implementation of full Monte Carlo dose calculation in proton beam therapy *Phys. Med. Biol.* 53 4825–53
Petti P L 1992 Differential-pencil beam dose calculations for charged particles *Med. Phys.* 19 137–49
Schaffner B, Pedroni E and Lomax A 1999 Dose calculation models for proton treatment planning using a dynamic beam delivery system: an attempt to include density heterogeneity effects in the analytical dose calculation *Phys. Med. Biol.* 44 27–41
Sakae T *et al* 2000 Multi-layer energy filter for realizing conformal irradiation in charged particle therapy *Med. Phys.* 27 368–373
Spezi E, Angelini A L, Romani F and Ferri A 2005 Characterization of a 2D ion chamber array for the verification of radiotherapy treatments *Phys. Med. Biol.* 50 3361–73
Szymanowski H *et al* 2001 Experimental determination and verification of the parameters used in a proton pencil beam algorithm *Med. Phys.* 28 975–87
Tachikawa T *et al* 1999 Proton beam therapy facilities of the National Cancer Center East Hospital *Radiat. Indust.* 84 48–53
Takada Y *et al* 2008 The basic study of a bi-material range compensator for improving dose uniformity for proton therapy *Phys. Med. Biol.* 53 5555–69
Waters L 2002 MCNPX user's manual version 2.4.0 *Los Alamos National Laboratory Report* LA-CP-02-408
Yepes P, Randeniya S, Taddei P and Newhauser W 2009 Monte Carlo fast dose calculator for proton radiotherapy: application to a voxelized geometry representing a patient with prostate cancer *Phys. Med. Biol.* 54 N21–8